Journal of Applied Fluid Mechanics, Vol. 16, No. 4, pp. 830-849, 2023.
Available online at www.jafmonline.net, ISSN 1735-3572, EISSN 1735-3645.
https://doi.org/10.47176/jafm.16.04.1535

Numerical and Experimental Investigation on Unsteady Flow and Hydraulic Radial Force of Low-Head Axial Flow Turbine

Y. Sunsheng[1, 3], I. Enema Ohiemi[1, 2†], P. Singh[4], Y. Li[1], A. Ali [1] and F. Osman[5]

[1] *National Research Centre of Pumps, Jiangsu University, Zhenjiang 212013, China*
[2] *Department of Mechanical Engineering, University of Nigeria, Nsukka 410001, Nigeria*
[3] *Key Laboratory of Fluid and Power Machinery, Ministry of Education, School of Energy and Power Engineering, Xihua University, Chengdu, 610039, China*
[4] *Centre for Sustainable Technologies, Indian Institute of Science, CV Raman Road, Bangalore, India, 560012*
[5] *School of Energy Science and Engineering, Harbin Institute of Technology, Harbin 150001, China*

†*Corresponding Authors Email: israel.ohiemi@unn.edu.ng*

(Received August 27, 2022; accepted December 5, 2022)

ABSTRACT

Radial force in low-head axial flow turbines (AFTs) is an influential factor in their operational stability. To explore the transient operating behavior of the radial force in low-head AFTs under different blade numbers, transient numeric computations were executed with the shear stress transport (SST) *k-w* turbulent model. Turbine performance was numerically computed and compared with results from experiments. Furthermore, the unsteady flow field pulsations were experimentally verified by means of pressure sensors. The radial forces on the runners (z = 2, 3, and 4) were each numerically studied in time, frequency, and joint time–frequency fields. The result reveals that the radial force acting on the runner varies with time, since periodic radial forces reflect the vane number on the stay vanes with minimal runner effect. Moreover, the amplitude of the radial forces is directly proportional to the flow rate. Furthermore, the spectral analysis shows that the radial force frequency is close to the blade passing frequency and also increases radially outward since peak values were recorded in this region. Minimal radial force amplitudes were recorded when z = 3, across all flow conditions, making this configuration suitable for smooth and reliable operation. The unstable pressure and force pulses that affect the noise and vibration produced in the turbine are instigated by the flow exchange that occurs between the guide vane and the runner. In order to optimize turbines for increased operational dependability, the acquired data would be crucial references for noise and vibration analytical investigations.

Keywords: Axial flow turbine; Radial force; Blade number; Unsteady flow field; Performance; Pressure pulsation.

NOMENCLATURE

C_p	coefficient of pressure fluctuation intensity
D	diameter of runner
e	dissipation of kinetic energy of turbulence
$F1$	blending or auxiliary functions in turbulence model
f_n	shaft frequency
g	acceleration due to gravity
H	head
k	kinetic energy of turbulence
M	torque
n_s	specific speed
N	rotational speed
P	pressure
Q	flow rate
S	sample size
Γ	auxiliary variables in turbulence model
η	efficiency
ρ	density
δ_{ij}	Kronecker's delta
μ_T	turbulent viscosity
μ	dynamic viscosity

Subscripts

gv	guide vane
i, j	components in different directions
0	origin
x_i	cartesian coordinates: x, y, z

Abbreviations

AFT	Axial Flow Turbine

t	time
U_2	circumferential velocity of runner outlet
z	blade number
σ_k, σ_ω	turbulence-model coefficients
β^*, γ	turbulence-model coefficients
Δ	difference

AFP	Axial Flow Pump
BPF	Blade Passing Frequency
CFD	Computational Fluid Dynamics
3-D	three-dimensional
RANS	Reynolds-Averaged Navier–Stokes
SST	Shear Stress Transport

1. INTRODUCTION

Axial flow turbines (AFTs) are a crucial subset of turbomachines that effectively transform low-head water into mechanical energy, which is then transformed into electrical energy by connecting a generator. An important component of this type of turbine's design and operating life cycle is its performance behavior. Since its introduction and patenting by Viktor Kaplan in 1912 (Dixon and Hall 2013), its performance has been improved through optimization efforts by a host of researchers. The hydraulic design of AFTs is founded on the postulation of a free vortex and steady flow between the runner and guide vane on the basis of an infinite number of blades. However, the rotor and stator interaction (RSI) has the potential to excite forces on the runner irrespective of the flow condition (Jacquet-Richardet *et al.* 2013). The resultant effect of the exciting forces, together with forces from the fluid, influences blades, bearings, and shaft reliability (Rodriguez *et al.* 2007). The turbomachinery's fluctuating unsteadiness produces numerous excitation signals in the flow structures because it directly influences force fluctuation behavior (Ni *et al.* 2020). Pressure pulsations from the turbine's transient operation might lead to an uneven load variation on the runner (Amiri *et al.* 2015). As a result, the turbine's lifespan is shortened, pressure loss is increased, and its overall efficacy is decreased (Amiri *et al.* 2015; Harding and Richmond 2017).

It is a complex process to theoretically solve the hydrodynamic forces acting on the runner of a turbine (Agostinelli *et al.* 1960; Iversen *et al.* 1960). Zhu *et al.* (2006) used CFD to outline the dominant failure effect of Reynolds shear stress on an axial flow blood pump. The relationship between shear stress and static pressure was established by Yasuda *et al.* (2001). The lateral runner excitation in the vaneless region was examined by Agostinelli *et al.* (1960). According to an experimental study of pulsating pressure in turbomachines at various flow scenarios, the highest amplitudes are seen in transient operations. (Houde *et al.* 2012; *Trivedi et al.* 2014; Amiri *et al.* 2015; Harding and Richmond 2017). The guide vane of an AFT has a significant influence (Rivetti *et al.* 2014) on the pulsations within its flow channel, irrespective of its axial distance from the runner (Greitzer *et al.* 2004; Rivetti *et al.* 2014).

According to Dörfler *et al.* (2013), the RSI essentially produces the stimulation of a distinct pattern of runner vibration. The interplay of the foregoing cascades is expressed by the sensitive interchange of periodic forces, main frequency, and harmonics depending on the blade number in each flow domain and the shaft speed (ISO_354 2003; Dörfler *et al.* 2013).

Using several turbulence models, Javadi and Nilsson (2017) numerically presented a thorough RSI analysis on AFTs. Kim *et al.* (2019) used fast Fourier transform and unsteady flow modeling to explore the influence of flow patterns on an AFT's tip clearance under various flow conditions. Sang *et al.*'s (2017) numerical study of the RSI of the radial forces was supported by large eddy simulation in a two-stage AFP.

AFT performance and unsteady pressure pulsations were experimentally explored by Ohiemi *et al.* (2022). They came to the conclusion that an ideal axial gap is necessary for optimum turbine performance and safe operation of the turbine.

Zhang *et al.* (2019, 2020) numerically investigated the failure of an AFT, validated the obtained results by modal analysis, and compared the natural frequencies of the runner with a faulty one. Shamsuddeen *et al.* (2020) used an anti-cavity fin to investigate the effects of cavitation on an AFT's tip clearance. Song and Liu (2019, 2020) investigated how floor vortex impacts fluctuations in pressure of an AFP. Shi *et al.* (2021) studied the variation in the pressure of an AFP and a tubular pump. Compared to the AFP, the entry point of the tubular pump registered peak fluctuations in pressure.

Cui *et al.* (2020) predicted the radial forces and energy vibration on a centrifugal pump using a CFD model, and their experimental results were in agreement with CFD, making a strong case for radial force prediction. Similarly, Kruger *et al.* (n.d.) investigated the hydrodynamic radial forces on the blades of a vertical mixed pump using CFD, and their experimental results are consistent with CFD. The findings above clearly support the reliability of CFD in predicting and analyzing transient hydrodynamic force.

Pochylý *et al.* (2016) developed a novel swirl turbine as a variant of low-head AFTs that can operate at 1-6 m, suitable for small rivers with the capacity to operate as a tidal turbine.

Additional research is required since the blade number is a crucial parameter. Haluza *et al.* (2002) developed a two-blade AFT runner for low-head and large-flow applications with excellent flat efficiency curves and cavitation properties

A number of researchers investigated the effect of blade number on the performance characteristics of various turbomachines (Abo Elyamin *et al.* 2019; Ketata *et al.* 2020; Li *et al.* 2020; Yu-qin and Ze-wen

2020; Eltayesh *et al.* 2021). For AFTs, Šoukal *et al.* (2015) developed a model axial hydraulic turbine with four distinct rotors (R1 with z = 8, R2 with z =8, R3 with z = 4, and R4 with z =4) with the same 80 mm diameter. They further concluded that R2 (optimized) had the highest energy utilization coefficient and maximum efficiency.

In their experimental study of the effects of blade number and height on the performance of a low-head AFT, Singh and Nestmann (2011) concluded that blade number has a greater impact on the performance of the AFT than does blade height. Similar to this, Byeon and Kim (2013) looked at the impact of geometrical factors under various speed situations and concluded that blade number has the most significant impact on rotational speed.

1.1 Research Gap

The reviewed literature on AFTs shows that previous studies on blade number were basically on external flow characteristics such as performance. Blade number is an essential design parameter and has diverse effects on the internal flow characteristics, such as unsteady flow field and radial forces, which could significantly affect the stable operation of the AFT. For low-head AFTs, blade number effect on the unsteady flow fields, including radial force, has not been investigated. This work was designed to explore a low-head AFT's unsteady flow and hydraulic radial force computationally and experimentally. To investigate the effect of blade number on unstable fluctuations and hydraulic radial force of AFT under various flow conditions, AFT model testing and numerical analysis utilizing the Shear Stress Transport (SST) turbulence model were investigated. The relative speed of the runner and the strength of the pulsing pressure were also investigated. In order to better highlight the RSI and the impact of blade number on unstable radial force on the AFT's runners, the time-series radial force signals produced from numerical simulations were analyzed using the FFT. The results from this investigation would be a vital design reference point for future AFT designs and an operational safety guide for the turbine, since it will provide relevant data on the effect of blade number on unsteady flow radial force and help operators to know the adequate blade number to use during turbine operation.

1.2 Research Goals

1) To numerically study an AFT's unsteady flow field under different runners (z = 2, 3, and 4) and validate the numerical computations through model tests. This consists of installing a pressure sensor on the AFT to validate the numerical unsteady flow pressure fluctuations computed using the SST *k-w* turbulence model for different flow rates.

2) To examine and compare the runners' internal distribution of pressure and velocity flow intensities. Furthermore, the pressure on vital parts of the runners was monitored and statistically compared in the form of time-series and joint time–frequency analysis to reveal the periodic signature and the harmonic patterns within the flow channels of the AFT.

3) To quantitatively analyze the impact of blade number on hydraulic radial force and evaluate it in relation to the pulsation patterns of the various blade numbers.

2. NUMERICAL METHOD

2.1 Turbine Model

The turbine model under investigation is presented in Fig. 1. The 3D models of the turbine were modelled using CREO parametric software.

The guiding vane, the runner, and the intake and exit pipes make up the turbine. Using the free vortex theory, three runners of the axial flow turbine model were created, each with the identical guide vane, outlet, and input pipe (Singh and Nestmann 2009, 2010, 2011; Li *et al.* 2022) and a particular speed of 728 metric (see Eq. (1) and Appendix A1).

$$n_s = \frac{N\sqrt{P_{hp}}}{H^{5/4}} \tag{1}$$

Three runners (z = 2, 3, and 4) with a 0.5 mm tip clearance was used. With nine (9) vanes, the guiding vane rotates at a speed of 1450 rpm. See Table 1 for turbine geometric parameters.

2.2 Pressure Fluctuation Intensity

Statistical procedures are required to compute the pressure fluctuation coefficient for each individual grid in the flow domains. These methods will aid in describing the zones of very unstable flows in the AFT geometry. Feng *et al.* (2006, 2007) used the instant pressure, p, at each grid node to be decomposed into two pressure variables, as expressed in Eq. (2) and (3): the periodic pressure variable, $\tilde{p}$, which is determined by the periodic difference in the blade passing frequency (BPF), and the time-averaged variable, $\bar{p}$.

Time-Averaged Pressure Variable,

$$\bar{p}(node) = \frac{1}{S}\sum_{J=0}^{S-1} P(\text{node}, t_0 + j\Delta t) \tag{2}$$

Periodic Pressure Variable,

$$\tilde{p}(node,t) = p(node,t) - \bar{p}(node) \tag{3}$$

The pressure is then normalized with regard to fluid density and tip velocity using Eq. (4) to estimate a non-dimensional pressure fluctuation intensity coefficient, C_p, of all the grids in the nodes in one period.

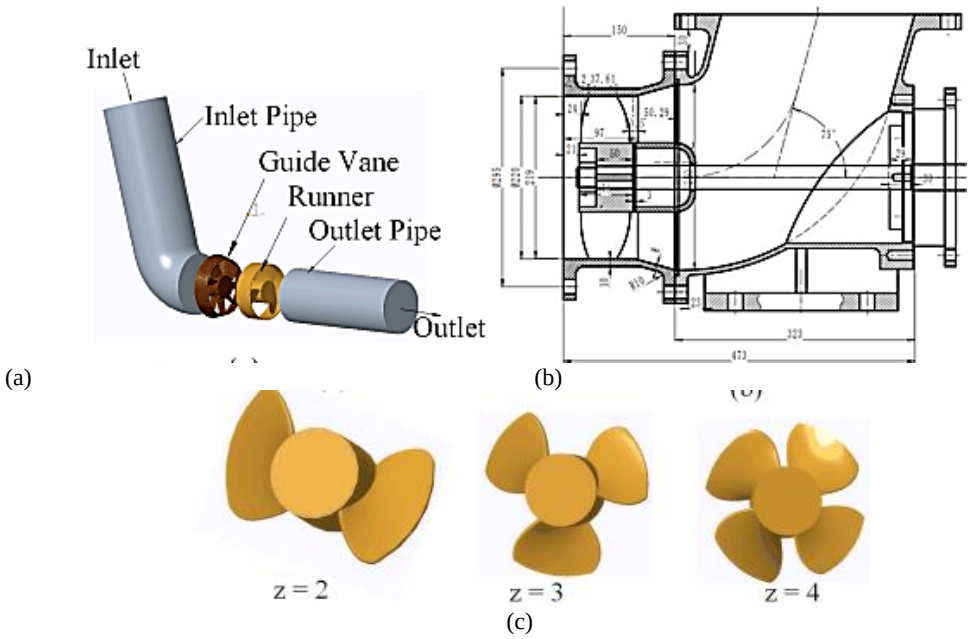

Fig. 1. Structural Model of low-head axial flow turbine (a) 3D turbine model; (b) 2D sectional view of the low-head AFT; (c) runners.

Table 1. Model Specification.	
Specification	
Specific Speed n_s (metric)	728
Shaft Speed n (rpm)	1450
Discharge (l/s)	196
Guide Vane Numbers z_{gv}	9
Diameter of runner (mm)	218
Blade number z	2, 3, and 4
Tip Clearance (mm)	0.5
Guide Vane Inlet Diameter (mm)	250
Guide Vane Outlet Diameter (mm)	200
Axial Gap (mm)	10

$$C_p = \frac{\left(\frac{1}{S}\sum_{j=0}^{S-1}\tilde{p}(node, t_0 + j\Delta t)^2\right)^{0.5}}{\frac{1}{2}\rho U_2^2} \tag{4}$$

In Eq. (4), S represents the sample size in one period and the initial time for the transient computations, while Δt and j signify time-step and number of timesteps, respectively.

2.3 Governing Equations

Water is used as the operating fluid. It is assumed to be unsteady, incompressible, and expected to flow in a 3D turbulent manner. To accurately predict the performance characteristics of a low-head AFT with special consideration to varying blade numbers, the unsteady Reynolds-averaged Navier–Stokes (URANS) equations for mass and momentum conservation is presented as

$$\frac{du_i}{dx_i} = 0 \tag{5}$$

$$\rho\left[\frac{\partial \overline{u_i}}{\partial t} + \frac{\partial\left(\overline{u_j}\,\overline{u_i}\right)}{\partial x_j}\right] = \frac{\partial}{\partial x_j}\left[\mu\left(\frac{\partial \overline{u_i}}{\partial x_j}\right) - \rho\overline{u'_j u'_i}\right] - \frac{\partial \overline{p}}{\partial x_i} \tag{6}$$

The term $-\rho\overline{u'_j u'_i}$ represents the Reynolds stress tensor and is defined as

$$-\rho\overline{u'_j u'_i} = \mu_t\left(\frac{\partial \overline{u}_j}{\partial x_i} + \frac{\partial \overline{u}_i}{\partial x_j}\right) - \frac{2}{3}\delta_{ij}\left(\rho k + \mu_t \frac{\partial \overline{u}_k}{\partial x_k}\right) \tag{7}$$

The Kronecker delta (δ_{ij}) is defined as

$$\delta_{ij} = \begin{cases} 1 \; for \;\; i = j \\ 0 \; for \; i \neq j \end{cases} \quad i, j = 1,2,3.$$

2.4 Turbulence Model

The SST k-ω model was used to resolve the flow equations in the AFT. The suitability of SST k-ω in predicting the flow behavior within hydraulic machinery has been established by several researchers (Božić and Benišek 2016; Sotoude Haghighi *et al.* 2019, 2020). Menter (1993) and Wilcox (1994) comprehensively proved the SST model as an improved k-ω turbulence model. Menter (1993) further developed a function to blend the model proposed by Wilcox (1994), since it is susceptible to free-flowing stream. SST is a

combination of the modified *k-ω* and *k-ε* equations that smoothly switch between free stream flow and the inner wall layer by using blending functions.

Transformed $k-\varepsilon$ *model*:

$$\frac{\partial(\rho k)}{\partial t}+\frac{\partial}{\partial x_j}(\rho U_j \mathrm{k})=\frac{\partial}{\partial x_j}\left[\left(\mu+\frac{\mu_t}{\sigma_{k2}}\right)\frac{\partial k}{\partial x_j}\right]+P_k-\beta'\rho k\omega \tag{8}$$

$$\frac{\partial(\rho\omega)}{\partial t}+\frac{\partial}{\partial x_j}(\rho U_j\omega)=\frac{\partial}{\partial x_j}\left[\left(\mu+\frac{\mu_t}{\sigma_{\omega 2}}\right)\frac{\partial\omega}{\partial x_j}\right]+2(1-F_1)\rho\frac{1}{\sigma_{\omega 2}\omega}\frac{\partial k}{\partial x_j}\frac{\partial\omega}{\partial x_j}+\alpha_2\frac{\omega}{k}P_k-\beta_2\rho\omega^2 \tag{9}$$

The blending functions F_1 and F_2 are as follows:

$$F_1=\tanh(\Gamma_1^4) \tag{10}$$

$$F_2=\tanh(\Gamma_2^2) \tag{11}$$

Eq. (12) was used to evaluate turbulent viscosity, μ_t:

$$\mu_t=\frac{\alpha_1 k\rho}{\max(\alpha_1\omega, SF_2)} \tag{12}$$

The *k-ω* equation is suitable for the prediction of flow within internal walls with constants β'=0.09, σ_{k1} = 1.176, $\beta 1$ = 0.075, $\sigma_{\omega 1}$ = 2.0, and α_1 = 5/9, while β_2 = 0.828, $\sigma_{\omega 2}$ =1/0.856, and σ_{k2} = 1.0 were used for the free stream (ANSYS 2020; Huang *et al.* 2021; Li *et al*. 2022).

2.5 Grid Generation

Figure 1 shows the flow domain of the turbine under consideration. To achieve numerical correctness, structured (hexahedral) grids made from a multiple block structure were actualized using ANSYS ICEM CFD. It was subsequently improved with additional grids to measure the complicated flow environment since the region around the RSI is essential to numerical accuracy. The mesh quality and density were increased and improved using the O-Grid method. In order to prevent flow reversal, the exit and input pipes were adequately expanded.

The grid-independent study was performed at Q_d, the design flow rate, using z = 3. Six grids was considered (see Fig. 3).

Considering computational resources and the need for the least amount of variation, Grid C, with its 7.5×10^6 cells (runner: 2.8×10^6, output pipe: 1.0×10^6, inlet: 1.0×10^6, and guide vane: 2.3×10^6), was chosen (Celik *et al.* 2008). The remaining runners (z = 2 and 4), were subjected to the same procedure but approximate cell sizes in order to be consistent with the grid-sensitivity analysis while the head was computed using Eq. 13 as depicted in Table 2 and Fig. 2.

$$H=\frac{P_{out}-P_{in}}{\rho g} \tag{13}$$

Table 2 Grid-Independent Studies.

Grid	Grid Number ($\times10^6$)	Head (m)	Grid Convergence Index (GCI) (%)
1	5.50	3.95	3.9432
2	6.50	4.30	2.6324
3	7.50	4.50	1.9875
4	8.50	4.52	1.9879
5	9.0	4.518	1.9878
6	9.5	4.518	1.9877

2.6 Steady and Unsteady Simulations

The use of an adequate turbulence model is required to accurately predict the inner flow behavior of an AFT due to the complex nature of its flow patterns.

To meet this requirement, the 3D unstable RANS equation was solved using the standard SST model and ANSYS CFX. The frozen-rotor interface was utilized to analyse the flow at the runner's interface under steady-state conditions. The following pressures were used: 1000 Pa for the total pressure, 1 atm for the reference pressure, and 5% for the turbulence intensity. At the output, a mass flow rate was chosen and changed under part-load, design-load, and overload flow circumstances. The inside

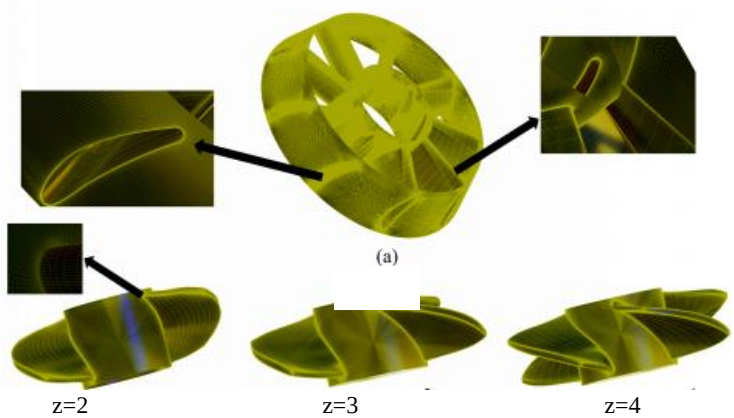

Fig. 2. Component mesh: (a) guide vane (b) investigated runners.

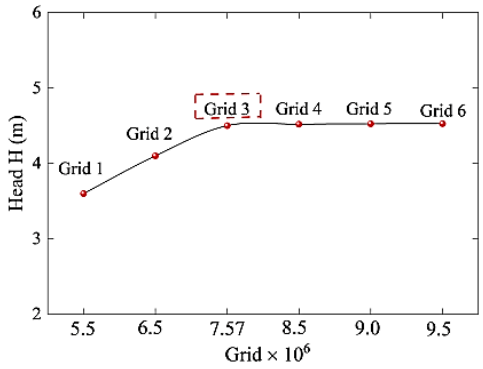

Fig. 3. Grid sensitivity analysis.

wall pattern was non-slip. The general grid interface (GGI) was utilized to ensure that there was never any conflict between non-matching nodes because different mesh terrain angles are unavoidable.

After a thousand cycles, steady-state simulations were unable to identify the AFT's flow characteristics. Because of this, the transient-state computations began using the steady-state simulation results and modify the mesh positions at each time-step using the transient-rotor-stator. A time-step of 0.00011 s was set for 1° of the runner rotation since it may be used to obtain the necessary time resolution. For z = 2, 3, and 4, respectively, a total times of $0.0828, 0.124,$ and 0.166 s, respectively were observed for 2, 3, and 4 full runner revolutions. With ten (10) flow iterations per time-step, the time was correctly discretized. With a residual objective of 10^{-5}, the root mean square (RMS) was also carefully selected.

3. EXPERIMENTAL METHOD

The turbine with three runners (z = 2, 3, and 4) was made and utilized to validate the numerical calculations. An electromagnetic flow meter (OPTIFLUX 2000F), three water tanks, pressure transmitters (Yokogawa EJA), butterfly valves, and sophisticated sensors are all parts of the close-loop test equipment, which was utilized to verify the CFD results. The flowmeter is situated at the level of -2.6 m in the test bed, which is made up of the lower and upper floors. The flow rate and differential head were measured using the OPTIFLUX 2000F with 0.2% and 0.1% error, respectively, and the Yokogawa EJA. We measured the torque and speed using a JCL1/200 Nm intelligent torque transducer. The pressure pulsations were measured using intelligent pressure sensors with an error of less than 0.1%. The rig's overall accuracy is 0.3%, and it is consistent with IEC 60193-1999 requirements. Additionally, a total uncertainty of 1.223% for the entire experiment was calculated (see Appendix A2). The experiment was conducted using a shaft speed of 1450 rpm. Figure 4 depicts the experimental setup. The test rig instrumentation and the location of CY 200 is shown in Fig. 5)

In order to actualize the A/D amplification, transition, rectification, and filtration, among other signals detected by sensitive components, the CY200 integrates a single-chip made from a piezoresistive silicon crystal, fully utilizing their retention and processing potentiality. The digital pressure signals were saved on the associated computer for imminent analytical study. The detection of a sample frequency (f_s) of 1000 Hz and period (T) of 20 s occurred after the turbine had stabilized in its operational state.

The frequency being studied is within the range of the Nyquist frequency ($0 \sim 441.7\ Hz$). CY200 pressure sensors were mounted at the guiding vane at P2. The sensor was connected to the hub for transmission and then to the console. Following the opening of the pneumatic valves to the specified flow rate, the time-series pressure pulses were captured. The process was carried out once again for diverse flow conditions, and the resulting time-series fluctuating pressure was recorded.

4. RESULTS AND DISCUSSION

4.1 Pressure Pulsation Comparative Analysis: Numerical Experiment

FFT was utilized to generate the frequency-domain data from the transient signals obtained from the CY200 in order to thoroughly examine the fluctuating flow in the AFT. The obtained signals (CFD and experiments) were analyzed using the FFT technique after normalizing the pressures with Eq. 16. The frequency spectrum at $0.8Q_d$, $1.0Q_d$, and $1.3Q_d$ for all the investigated runner cases is displayed in Fig. 6 to study the relationship between the C_p of the test and CFD.

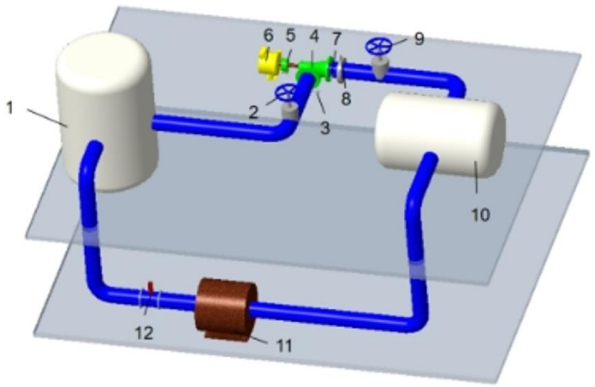

1. High-Pressure Tank
2. Control Valve 1
3. Import pressure transmitter
4. Water Turbine
5. Torque Speed Sensor
6. Generator
7. Outlet pressure transmitter
8. Exhaust valve
9. Regulator valve
10. Low-pressure tank
11. Booster pump
12. Flow meter

Fig. 4. Experimental Setup.

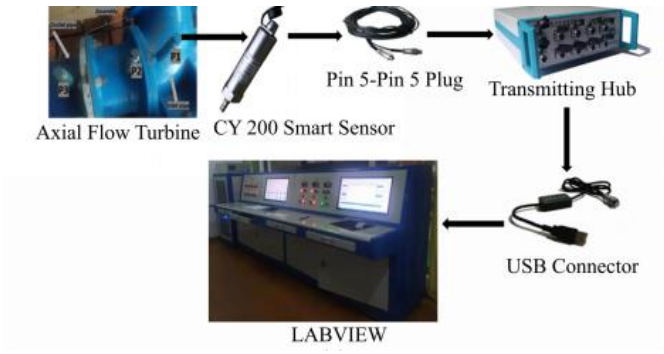

(a)

(b)

Fig. 5. Test rig instrumentation and Location of Pressure Sensors.

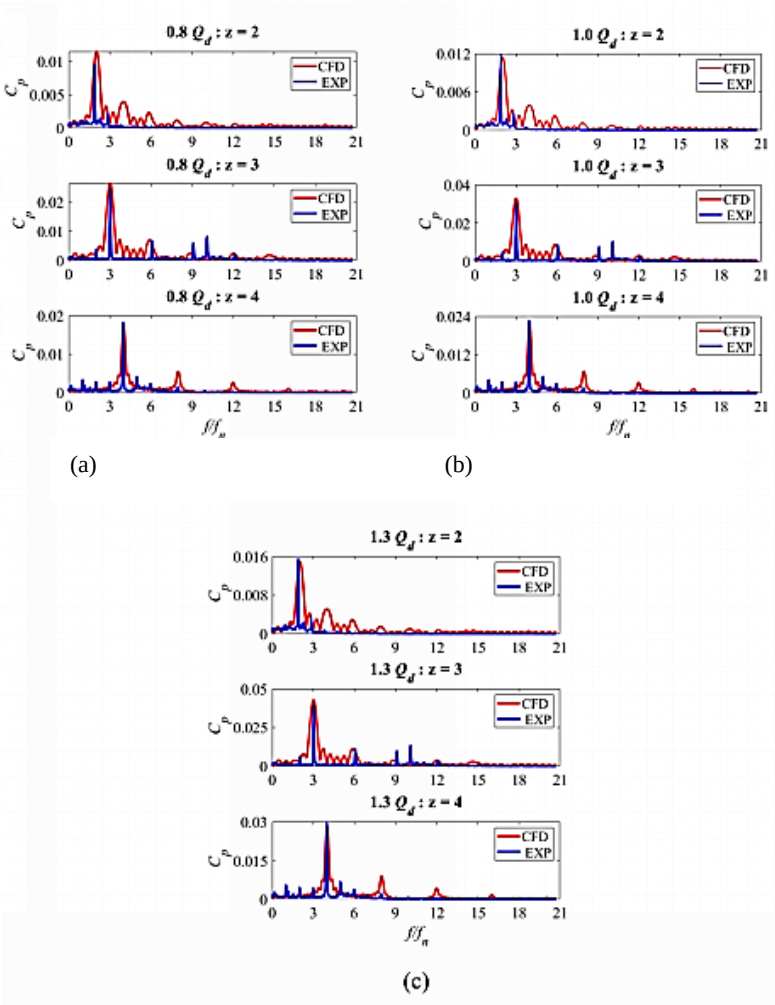

Fig. 6. Experimental and Numerical Frequency Spectrum at (a) 0.8Q_d; (b) 1.0Q_d; and (c) 1.3Q_d.

The experimental results and the CFD values differ slightly. Across all flow scenarios and blade assembly, the variance margin rises at higher frequencies.

The outcomes demonstrate a qualitative concordance between the CFD and model test findings (see Fig. 6). Furthermore, there is some agreement between the test results and the primary frequencies acquired from the CFD data. These conclusions were reached: First, when z is changed from 2 to 4, the major amplitude of C_p at P2 increases.

Second, although the numerical C_p are in agreement with test results at the BPF, larger disparities were observed at higher frequencies. The discrepancies between CFD and experimental data recorded at the main frequency is presented in Fig. 7.

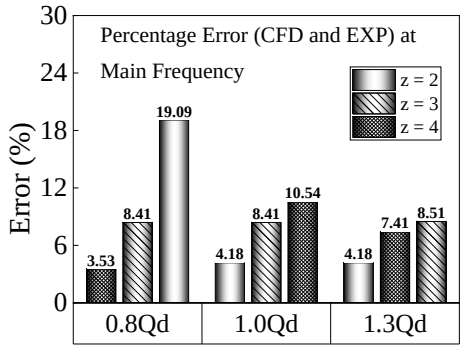

Fig. 7 Discrepancies between CFD and Experiment at the Main frequency.

Vibrations cause the aforementioned discrepancies in the AFT during the model test, which considerably heightens the complex nature of the flow characteristics in the AFT. The quantitative concordance between the CFD and model test shows the suitability of numeric results for further examination.

4.2 Internal Flow Characteristics

4.2.1 Relative Pulsating Velocity

The dispersion of velocity fluctuation intensity in the static vanes of the case study runners was analyzed using Eq. (14).

$$v_f = \frac{V_t}{U_2} \tag{14}$$

where V_t represents the timestep-dependent velocity and U_2 is the circumferential velocity at the runner's tip.

Figure 8 represents the runner's relative velocity intensity for all blade configurations. Higher v_f values were recorded at the leading edge (LE) but diminished as the flow progressed within the flow cascade to its lowest value at the trailing edge (TE). The v_f recorded at the suction side (SS) of the runner blade registered very low relative velocity fluctuation intensity as compared to the pressure side (PS). These occurrences can be attributed to flow circulation due to runner rotation. Extreme relative velocity fluctuation was recorded at the runner's leading edge for all the runner cases.

4.2.2 Pressure Pulsation Coefficient

The RSI generates large-pressure fluctuations with amplitudes more significant than all other turbine flow domains. To effectively delineate the flow characteristics in the runner, a statistical method was adopted to compute the C_p on every grid in the flow domains to characterize flow zones with high unsteadiness. The internal flow of the AFT under different blade numbers, z =2, z =3, and z =4, was analyzed to reveal the effect of blade number variation and flow rate on the AFT, as presented in Fig. 9. According to the C_p distribution shown in Fig. 8, there is a steady decline from the LE to the runner's TE. It was discovered that the PS of the blade experiences greater static pressure than the SS. Therefore, the rotation of the runner is caused by the pressure difference between the PS and the SS. The C_p on the runner decreases from the LE to the TE. The trailing edge recorded the least static pressure value within the runner flow domain. The above occurrence is due to the energy conversion process from the flowing fluid (potential energy) to the blades of the runner (kinetic energy). Furthermore, C_p within the AFT rises with a rise in flow scenario from $0.8Q_d$ to $1.3Q_d$.

4.2.3 Time-series Pressure Pulsations

The contour plots in the figure are insufficient to characterize the distribution of flow in the AFT; hence, it is necessary to investigate the flow behavior in the AFT quantitatively. Four monitoring points, LE, PS, TE, and SS, representing the blade leading edge, pressure side, trailing edge, and suction side, respectively, were placed on the tip profile of the investigated runners as presented in Fig. 10.

Figure 11 outlines the time-series of C_p for the respective runner revolutions when z = 2, 3, and 4 at $1.0Q_d$ for four (4) different monitored points.

Nine (9) peaks and troughs were recorded in the time-series plots for one period as the runner rotated through the respective revolutions following considered blade number. The time-series plot are inconsistent throughout the monitoring points, since LS and PS recorded more regular peak-to-peak plots across the flow rates from $0.8Q_d$ to $1.3Q_d$ (see Fig. 11). Irregularities in time-series signals were recorded at TE and SS. In general, nine (9) peaks and troughs were observed for one runner revolution, which corresponds with the vane numbers on the stay vane. Furthermore, the runner's blade number pattern was observed for one revolution for the different blade numbers. This effect is visible at LE and PS but challenging to identify at TE and SS across all flow conditions (see Fig. 11). The above scenario highlights the RSI influence since the signatures of both blade numbers on the runner and

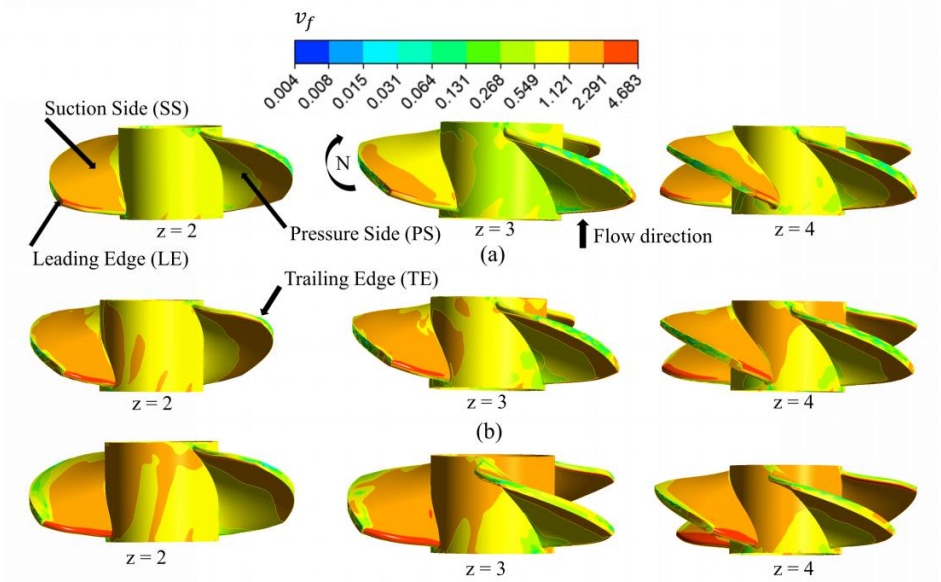

Fig. 8. Distribution of Velocity Fluctuation (v_f) within the Runner at (a) $0.8Q_d$ (b) $1.0Q_d$ (c) $1.3Q_d$.

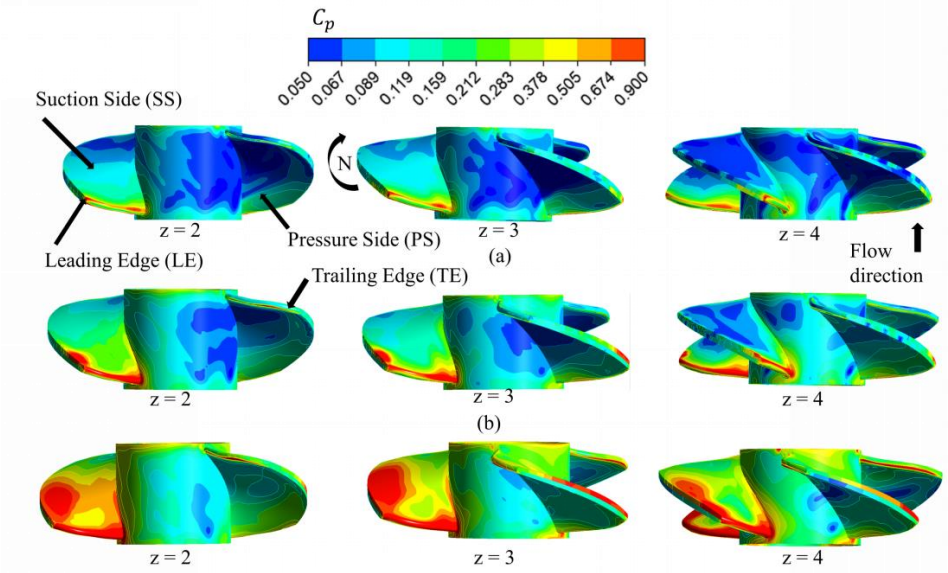

Fig. 9. Pressure Pulsation C_p on the Runner at (a) $0.8Q_d$; (b) $1.0Q_d$; and (c) $1.3Q_d$.

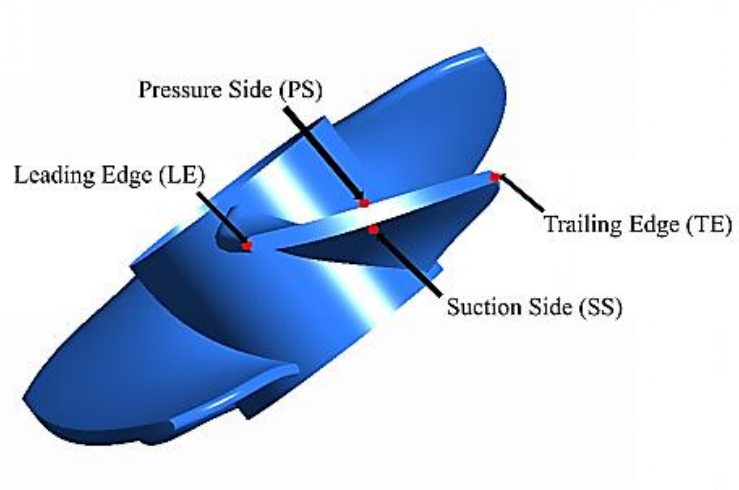

Fig. 10. Location of Monitored Points.

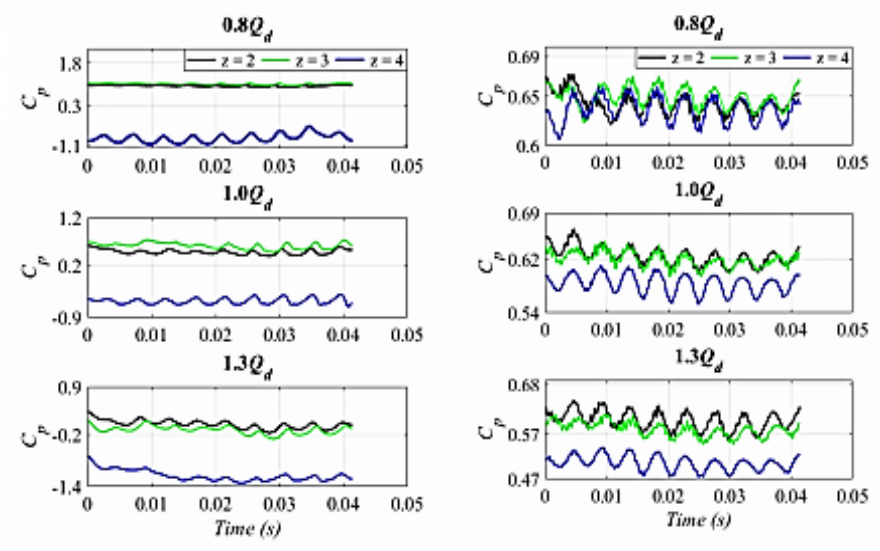

Fig. 11. Time-series signals of Cp at 0.8Q_d, 1.0Q_d, and 1.3Q_d: (a) Leading edge; (b) Pressure side; (c) Trailing edge; (d) Suction side.

guide vane are visible in the time-series plots of C_p (Dörfler *et al.* 2013; Rivetti *et al.* 2014). The C_p progressively decreases as the fluid flows from LE to TE. This reduction in C_p is attributed to the energy transition from the flowing fluid to shaft rotation in the form of mechanical energy.

The C_p at LE recorded the highest value across the four monitored points for all turbine configurations

(z = 2, 3, and 4).

However, because they are placed on the pressure side of the runner, the PS pulses are stronger than those at other sites. Additionally, the guide vane's peak flow momentum substantially impacts the runner's LE, resulting in a variety of complex flow interactions and peak C_p. With an increase in flow from 0.8Q_d to 1.3Q_d, C_p values fall at all places that are being monitored. Compared to runners in the other cases, z = 3 and 4, runner z = 2 showed the most extreme pressure fluctuation.

4.2.4 Periodic Pulsation Analysis in Time and Frequency Domain

Figures 12, 13, and 14 show the AFT's estimated unsteady combined time-frequency spectrum at various blade numbers. Only the runner can freely spin along its axis of rotation in the AFT. The runner sweep over the nine (9) guide vanes blades, all the locations of interest (TE, PS, TE, and SS) recorded frequency signatures in accordance with Eq. (15).

$$f_{i,c} = N \times Z_{gv} \times c \quad (c = 1, 2, 3, \dots) \tag{15}$$

The blade passing frequency would coincide with the lowest of $f_{i,c}$, when c =1, i.e., the harmonic number representing the excitation frequencies, and N is the shaft speed.

The runner is sensitive to the patterns of pressure of equiphase segments separated by nodal diameter

because of the uneven interface of the runner on the vane, particularly around the runner's perimeter,

however this is associated to the sort of harmonics (*k*, *c*) being evaluated. A detailed analysis of the peak signatures seen in the runner suggests that "c" is positive and in agreement with the rotation of the runner. 24.1667 *Hz* is the shaft frequency (f_s). Due to this, the runner's monitored points consistently registered nine (9) C_p troughs and peaks, which mimics the guide vane number, independent of the runner's blade number.

The excitation signatures recorded at TE and SS show irregular patterns different from the patterns recorded at LE and PS. The joint time–frequency analysis (see Figures 12, 13, and 14) reveals more clearly the irregularities recorded at both the SS and LE. The irregularities increase as the flow rate increases. The above shows that flow rate has a strong effect on pressure pulsations.

4.3 Hydraulic Radial Force on the runner

The forces acting on the runner under varied flow rates were monitored and studied by FFT (Shamsuddeen *et al.* 2020) in order to investigate the radial force obtained from RSI, which is presented in this section. F_x and F_y represent the two perpendicular components of the radial force F_r.

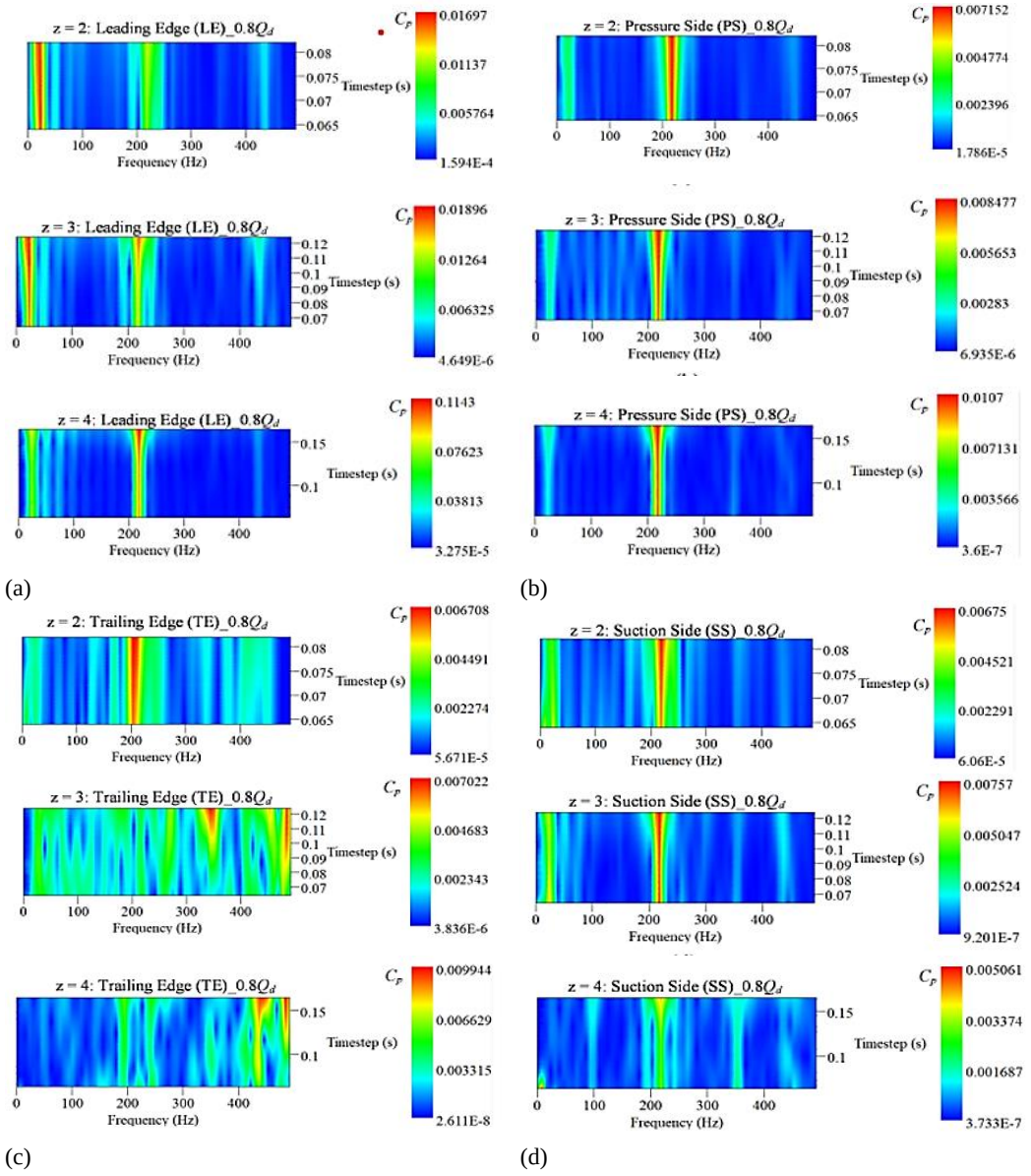

Fig. 12. Joint Time–Frequency Domain Analysis of *Cp* at 0.8Q_d: (a) Leading edge; (b) Pressure side; (c) Trailing edge; (d) Suction side.

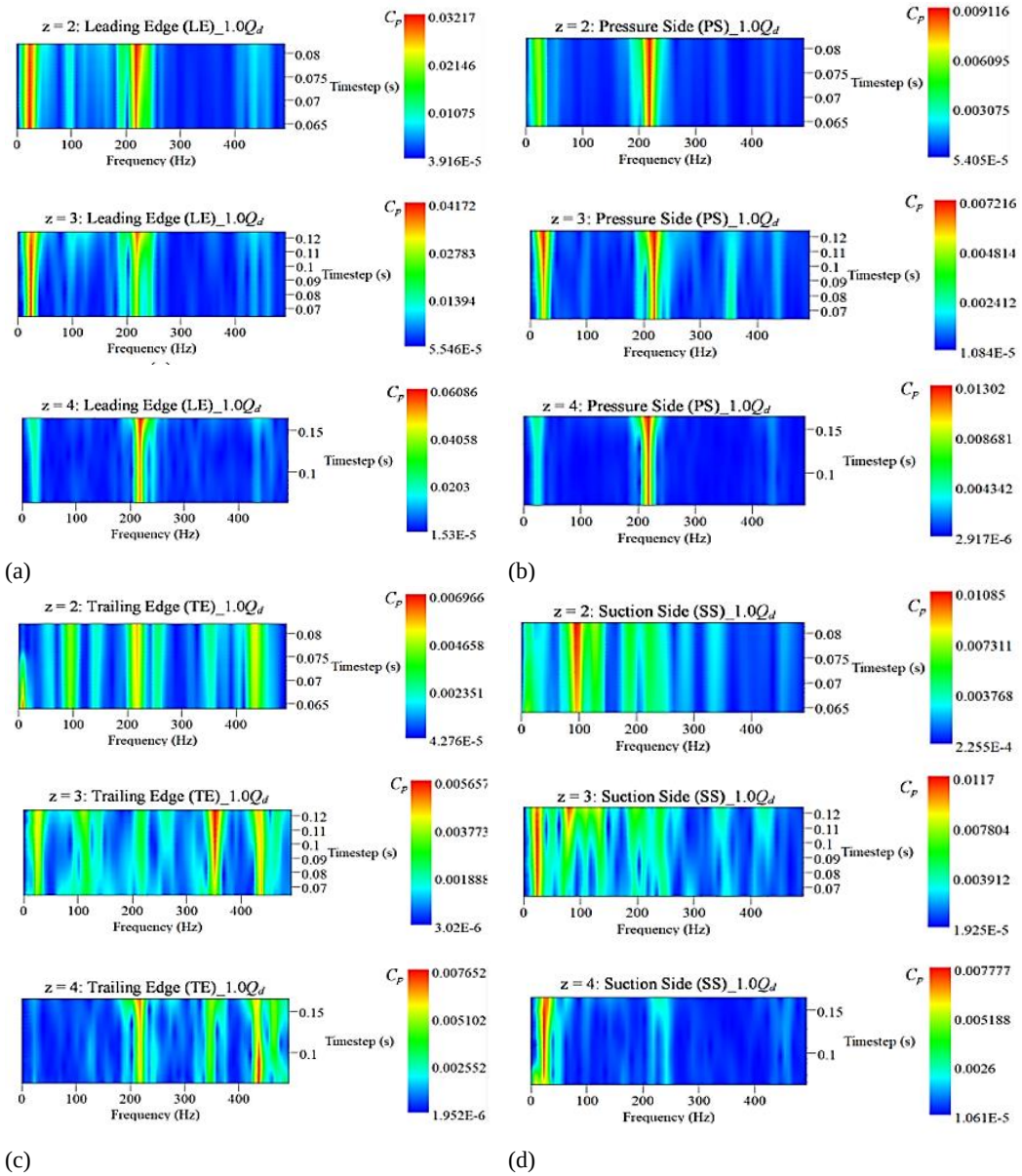

Fig. 13. Joint Time–Frequency Domain Analysis of C_p at 1.0Q_d: (a) Leading edge; (b) Pressure side; (c) Trailing edge; (d) Suction side.

4.3.1 Time Series of Unsteady Radial Forces

Figure 15 depicts the runners' comparative time-series radial force (z = 2, 3, and 4) at 0.8Q_d, 1.0Q_d, and 1.3Q_d. The angular axes show the runner's relative angular position in one rotation, while the radial axis shows the radial force F_r. The radial force has a diminishing and growing pattern under the effect of blade number (z = 2, 3, and 4), which can increase or reduce runner vibration and either enhance or worsen the bearing fatigue limit. The radial force achieves maximum magnitude when the runner rotates over the guide vane. Because the pressure distribution in the flow channel is uniform, the runner generates the least radial force at 0.8Q_d as compared to 1.0Q_d and 1.3Q_d. The runner's radial force rose slightly as the flow progressed to 1.0Q_d. The amplitude of the radial force increases significantly at 1.3Q_d. However, peak radial forces were recorded by z = 2 across all flow conditions, followed by z = 4. The radial force values recorded by z = 3 are minimal compared to the other runner configurations. The vector plot of the runner's irregular radial forces at different flow rates and for all AFT configurations under investigation is presented in Fig. 16. The origin of the coordinate frame represents the runner's spinning center. It is worth noting that the amplitude of the radial forces, together with their corresponding direction, fluctuates with runner rotation, and the form of the vector surrounding the curve is likewise quite irregular. The number of peaks and troughs on the

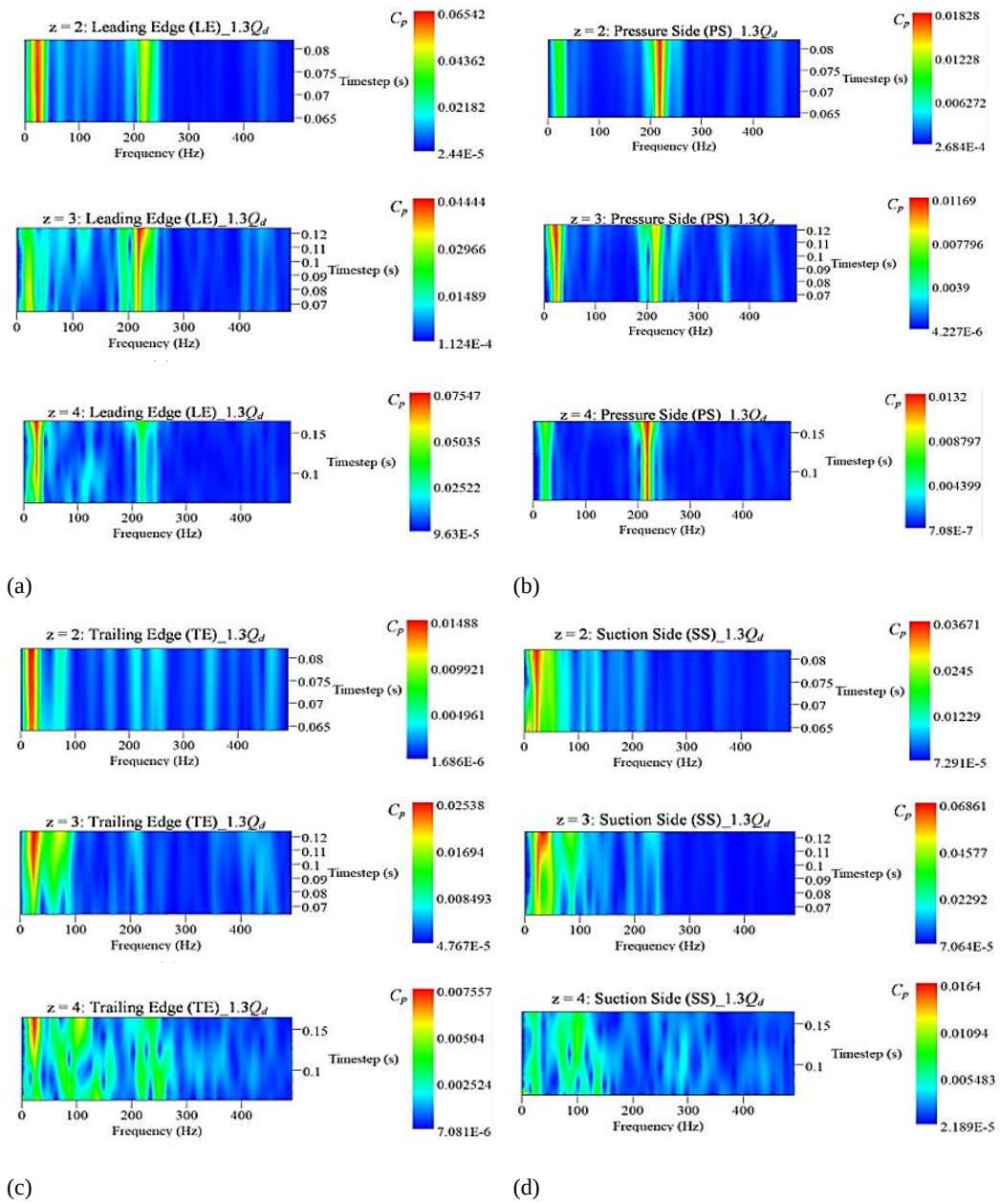

Fig.14. Joint Time–Frequency Domain Analysis of C_p at 1.3Q_d: (a) Leading edge; (b) Pressure side; (c) Trailing edge; (d) Suction side.

guide vane is inconsistent with the number of blades on the runners, indicating that the RSI influences the frequency component of radial force. The magnitude of the radial forces recorded by the time-series data for all the blades numbers is relatively small. The above result is consistent with what is obtainable with AFT.

4.3.2 Radial Force Distribution in the Frequency Domain

In line with the time series of radial force exerted on runners, FFT was used to analyze the frequency spectra of radial force on runners, and the frequency spectra of radial force under various operating conditions are shown in Fig. 17. The ordinate on the runner represents the radial force amplitude, while the abscissa depicts its frequency as a function of rotational frequency. The turbine's rotational frequency (RF) is $f_n = n/60 = 24.167\ Hz$ since the guiding vane number is z_{gv} = 9. As a result, the blade passing frequency is calculated as $f_n \times z_g = 24.167 \times 9 = 217.50\ Hz$ (BPF). The multiples of BPF and RF define other peaks in the spectrum. The radial force pulsation is most visible at low frequencies, as seen in the graph. Due to the impact of flow and RSI, the time-domain distribution of radial force is not regular, resulting in an uneven frequency domain distribution of radial force. When the dominant frequency is greater than 700 *Hz*, the

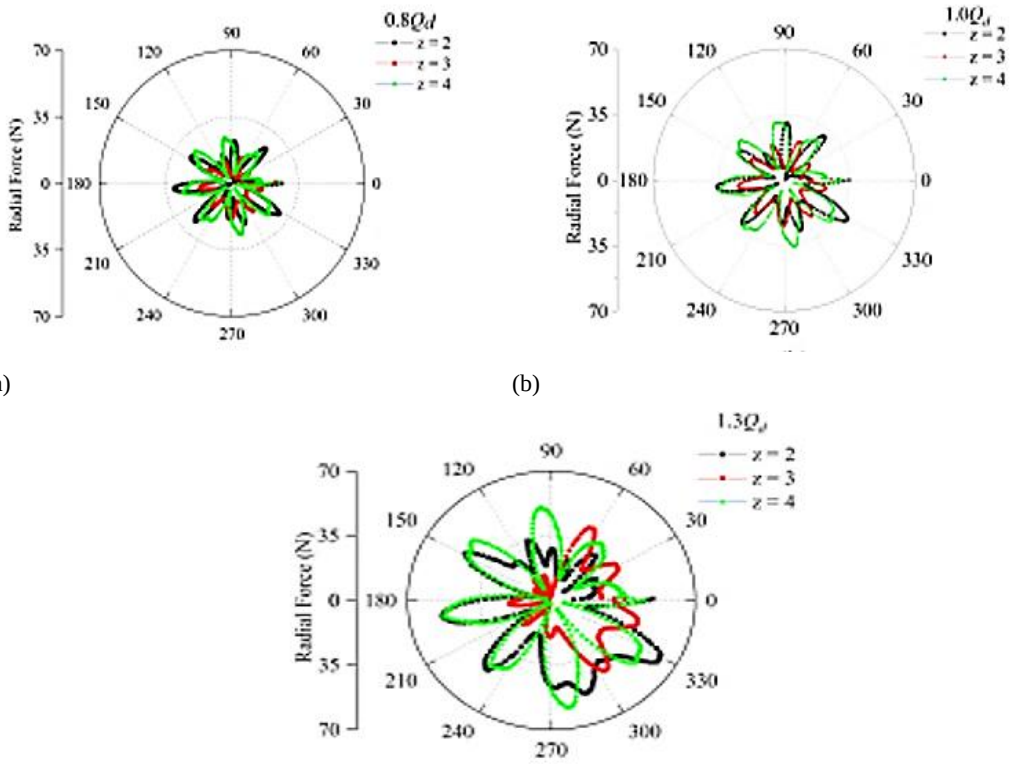

(a) (b)

(c)

Fig. 15. Time-series plot of Unsteady Radial Force: (a) 0.8Q_d; (b) 1.0Q_d; (c) 1.3Q_d.

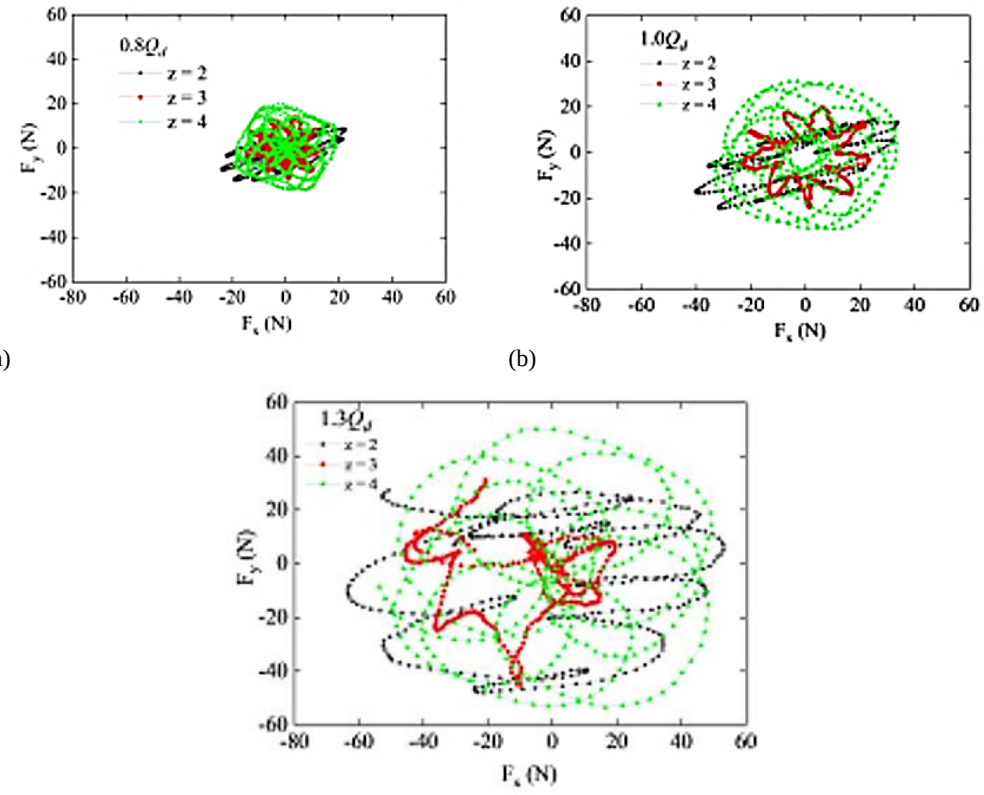

(a) (b)

(c)

Fig. 16. Vector Representation of Unsteady Radial Forces at (a) 0.8Q_d; (b) 1.0Q_d; (c) 1.3Q_d.

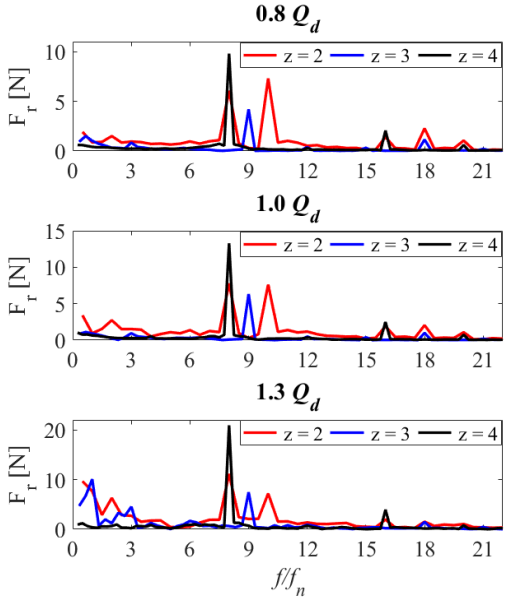

Fig. 17. Frequency Spectrum of the Radial Forces.

magnitude of the main frequency drops to the lowest value when the amplitudes are compared across all blade numbers.

Other peaks, on the other hand, show a decreasing trend with the effect of blade number on the guide vane, indicating that increasing the runner blade number can effectively reduce radial force pulsations and influence flow-induced vibration of the AFT. The amplitude of the radial force in the frequency domain falls from z = 2 to z = 3 when the flow condition increases from $0.8Q_d$ to $1.3Q_d$, then increases again at z = 4. z = 4 and z = 2 reported peak radial force values of 9.8 N and 7.3 N, respectively, at a flow condition of $0.8Q_d$. Peak radial force values of 7.8 N and 13.3 N were observed at $1.0Q_d$ z = 2 and z = 4, respectively. At $1.3Q_d$, peak radial force values of 11.2 N and 20.9 N were obtained for z = 2 and z = 4, respectively. The radial force values for z = 3 and z = 4 were the lowest across all case studies. In all flow circumstances, z = 4 created the most significant radial force in the frequency domain, followed by z = 2 and z = 3.

4.3.3 Joint time–frequency Analysis of Radial Force

The joint time–frequency domain analysis can reveal the transient characteristics of the dynamic radial force signals on the different runners. Figure 18 depicts a waterfall spectrum of the radial forces on the runners (z = 2, 3, and 4). When z = 2, intermittent amplitudes were observed with dual peaks at 193.3 Hz and 241 Hz around the main frequency of the radial force signals. Other amplitudes, which are multiples of the BPF, were observed in the spectra. The radial forces unswervingly displayed transient patterns. The main amplitudes for z = 3 and z = 4 occurred at 217.5 *Hz* and 193.3 *Hz*, respectively. As the blade number increases, the main amplitude of the discontinuous signals decreases significantly at z = 3 but increases at z = 4.

Nevertheless, intermittent amplitudes at higher frequencies gradually reduce, but a more stable main frequency trend is observed as time increases.

The joint time–frequency of the radial force in Fig. 19 is similar to the patterns observed at $0.8Q_d$. When z =2, large discontinuous amplitudes occur between 0 and 242 Hz. The main frequencies at z = 3 and 4 remain the same, with the patterns observed at $0.8Q_d$. The radial force only increases with an increase in flow rate, with z = 3 recording the lowest radial force values across the blade numbers.

Figure 20 shows the discontinuous amplitude of radial forces on a joint time–frequency domain spectrum. The patterns of radial force observed at $1.3Q_d$ are similar to those at $0.8Q_d$ and $1.0Q_d$, but differ as the main amplitude increases consistently with an increase in blade number. While the runner revolves, the blades are subjected to fluid forces of variable frequencies. When subjected to alternating loads, the blades and bearings are vulnerable to fatigue damage, which lowers the stability and lifespan of the turbine.

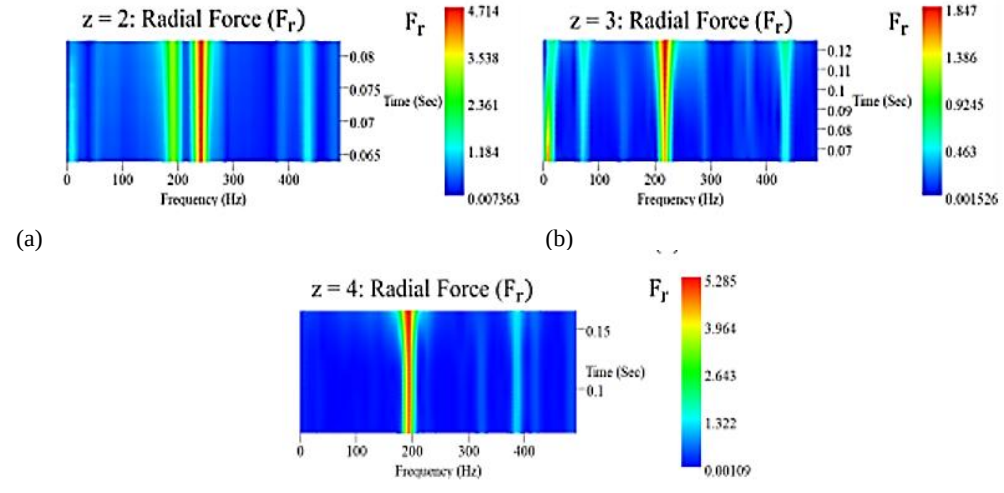

Fig. 18. Time–frequency Spectra of Radial Force on the runners at $0.8Q_d$ (a) z = 2 (b) z = 3 (c) z = 4.

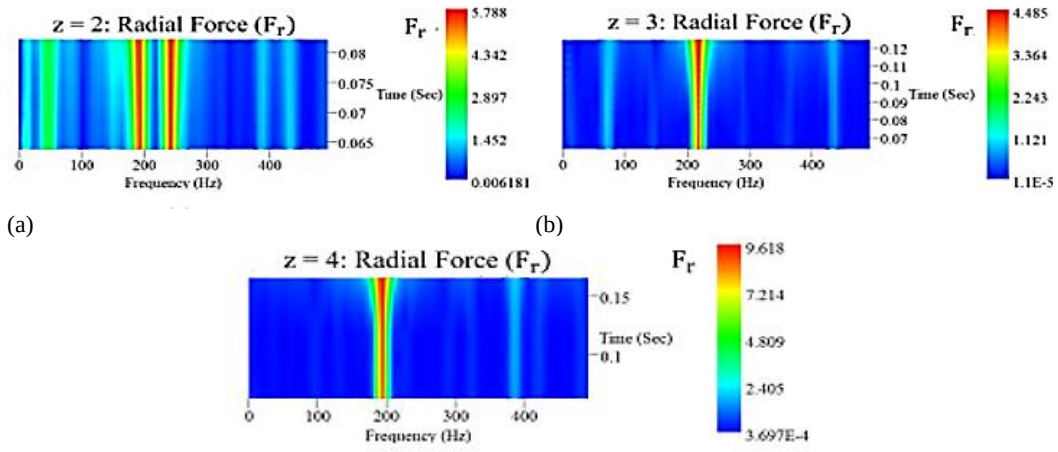

Fig. 19. Time–frequency Spectra of Radial Force on the runners at 1.0 Q_d: (a) z = 2; (b) z = 3; (c) z = 4.

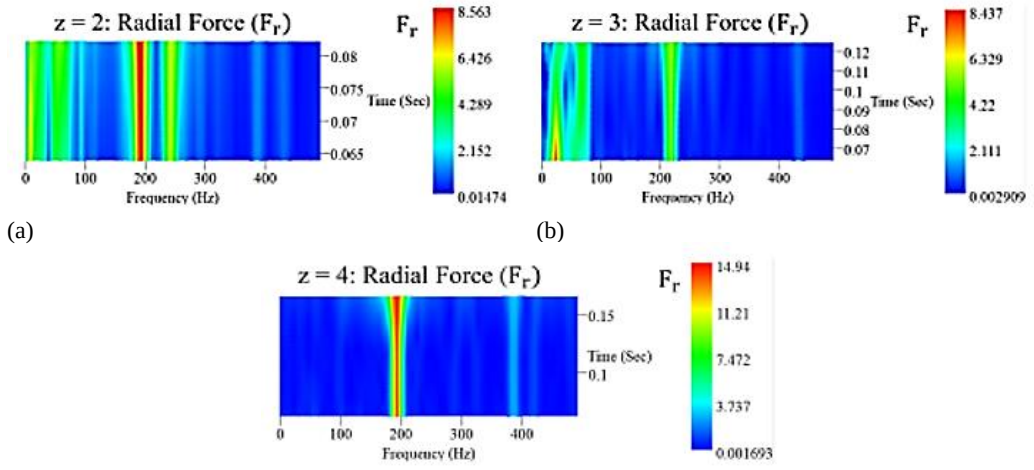

Fig. 20. Time–frequency Spectra of Radial Force on the runners at 1.3Q_d: (a) z = 2; (b) z = 3; (c) z = 4.

Changes in blade number and flow conditions have a significant impact on the radial force because of the RSI's unstable flow circumstances. However, for z = 2 and z = 4, the main frequency of radial force is close to the BPF, but a dissimilar trend was observed when z = 3, since the main amplitude occurred at the blade passing frequency and accounts for the lowest radial force values.

Consequently, for safety and turbine reliability, z = 3 is recommended since the runner would be subjected to fewer radial forces and hence less vibration, which would help prolong the runner bearing life and reduce turbine failures.

5. CONCLUSIONS

The impacts of blade number have been examined computationally and confirmed using an experimental method to examine the unsteady flow pressure pulsations and hydraulic radial stresses on the runners of the low-head AFT. To identify the unsteady flow features brought on by variations in blade number, spectra and combined time-frequency analysis were both applied. The following deductions were made:

1) The effect of blade number on unsteady flow field, and hydraulic radial forces on the runners of a low-head AFT was studied. Transient numerical studies of the performance and pulsating pressure intensities revealed by the monitored points depict a qualitative agreement with results from experiments conducted through the installed pressure sensors (CY 200).

2) Internal flow studies through contour plots and statistical coefficients of pulsating pressure on the runners, recorded by the time-series plots, frequency domain history, and joint time–frequency analysis, show an increasing trend from the blade leading edge to its trailing edge through the pressure surface. The pulsating signatures recorded by time-series signals for one runner rotation show nine (9) peaks and troughs for all the investigated blade numbers.

3) The frequency domain and joint time–frequency analysis of the runners revealed excitation frequencies such as 9 f_n, 18f_n, and 27 f_n. The blade passing frequency is primarily influenced by the number of vanes on the stay vane. The effect of the number of blades on the

runners is mainly on the pulsation signals recorded on the stationary parts, as revealed by the experimental data and numerically monitored points on the inlet, guide vane, and outlet pipes.

4) The radial forces recorded under part and design load conditions are minimal and more evenly distributed along the rotational axis of the shaft compared to the overload conditions where the distribution is irregular. Under all flow conditions, the radial force recorded by z = 3 is minimal, as revealed by the time and frequency history plots. Peak radial forces were recorded for z = 2 and z = 4, but a different trend was obtained at z = 3 since the smallest radial forces were recorded with this configuration. The excitation frequencies recorded by the radial forces on the runners of the AFT are close to the blade passing frequencies (BPF), as revealed by the frequency spectra, validating the influence of blade number on hydraulic radial force on the runners of the AFT.

Based on the results obtained in this investigation, the runner with z = 3 is recommended for low-head application since it recorded the lowest radial force for all flow conditions.

The method employed for this investigation can be applied to vibration diagnosis, which could help to understand further the forces acting on the runner of a low-head AFT. In order to optimize turbines for greater operational reliability, the obtained data would be crucial references for noise and vibration analytical studies.

ACKNOWLEDGMENTS

The authors disclose receipt of the following financial support for the research, authorship, and/or publication of this article: This research is funded in part by the Jiangsu Natural Science Foundation's youth fund project (Grant No. BK20180876), the major cultivation project of the Sichuan Provincial Department of Education (Grant No. 18cz0016), the Xihua University key project (Grant No. Z2010810).

DECLARATION OF COMPETING INTEREST

The findings presented in this research, according to the authors, were not influenced by any of their known financial conflicts of interest or close personal ties.

DATA AVAILABILITY

On request, the corresponding author will provide the information needed to substantiate the study's findings.

REFERENCES

Abo Elyamin, G. R. H., M. A. Bassily, K. Y. Khalil and M. S. Gomaa (2019). Effect of impeller blades number on the performance of a centrifugal pump. *Alexandria Engineering Journal* 58(1).

Agostinelli, A., D. Nobles and C. R. Mockridge (1960). An experimental investigation of radial thrust in centrifugal pumps. *Journal of Engineering for Power* 82(2), 120-125.

Amiri, K., M. J. Cervantes and B. Mulu (2015). Experimental investigation of the hydraulic loads on the runner of a Kaplan turbine model and the corresponding prototype. *Journal of Hydraulic Research* 53(4).

ANSYS CFX-Solver Theory Guide. (2020). http://www.ansys.com

Božić, I. and M. Benišek (2016). An improved formula for determination of secondary energy losses in the runner of Kaplan turbine. *Renewable Energy* 94, 537-546.

Byeon, S. S. and Y. J. Kim (2013). Influence of blade number on the flow characteristics in the vertical axis propeller hydro turbine. *International Journal of Fluid Machinery and Systems* 6(3).

Celik, I. B., U. Ghia, P. Roache and C. Freitas (2008). Procedure for Estimation and Reporting of Uncertainty Due to Discretization in CFD Applications. *Journal of Fluids Engineering*, 130(7), 078001.

Cui, B., J. Li, C. Zhang and Y. Zhang (2020). Analysis of radial force and vibration energy in a centrifugal pump. *Mathematical Problems in Engineering* 2020.

Dixon, S. L. and C. A. Hall (2013). *Fluid mechanics and thermodynamics of turbomachinery*, (7th edition). Butterworth-Heinemann.

Dörfler, P., M. Sick and A. Coutu (2013). *Flow-Induced Pulsation and Vibration in Hydroelectric Machinery*. Springer London.

Eltayesh, A., F. Castellani, M. Burlando, M. Bassily Hanna, A. S. Huzayyin, H. M. El-Batsh and M. Becchetti (2021). Experimental and numerical investigation of the effect of blade number on the aerodynamic performance of a small-scale horizontal axis wind turbine. *Alexandria Engineering Journal* 60(4).

Feng, J., F. Benra and H. J. Dohmen (2006). Numerical study on impeller-diffuser interactions with radial gap variation chair of turbomachinery. In *The 4th WSEAS International Conference on Fluid Mechanics and Aerodynamics*.

Feng, J., F K. Benra and H. J. Dohmen (2007). Numerical investigation on pressure fluctuations for different configurations of vaned diffuser pumps. *International Journal of Rotating Machinery* 2007, 1-10.

Greitzer, E. M., C. S. Tan and M. B. Graf (2004). *Internal Flow*. Cambridge University Press.

Haluza, M., P. Rudolf, F. Pochylý and F. Šob (2002). Design of a new low-head turbine. In *Proceedings of the XXI-St IAHR Symposium Hydraulic Machinery and Systems.*

Harding, S. F. and M. C. Richmond (2017). Experimental pressure measurements on hydropower turbine runners: a review of experimental methods to quantify hydropower turbine blade pressures at model and prototype scales. *Pnnl-26061* 48.

Houde, S., R. Fraser, G. Ciocan and C. Deschênes (2012). Experimental study of the pressure fluctuations on propeller turbine runner blades: part 2, transient conditions. *IOP Conference Series: Earth and Environmental Science* 15(6).

Huang, P., D. Appiah, K. Chen, F. Zhang, P. Cao and Q. Hong (2021). Energy dissipation mechanism of a centrifugal pump with entropy generation theory. *AIP Advances* 11(4), 045208.

ISO_354. (2003). International Standard International Standard. *61010-1 © Iec:2001* 13.

Iversen, H. W., R. E. Rolling and J. J. Carlson (1960). Volute pressure distribution, radial force on the impeller, and volute mixing losses of a radial flow centrifugal pump. *Journal of Engineering for Power* 82(2), 136-143.

Jacquet-Richardet, G., M. Torkhani, P. Cartraud, F. Thouverez, T. Nouri Baranger, M. Herran, C. Gibert, S. Baguet, P. Almeida and L. Peletan (2013). Rotor to stator contacts in turbomachines. Review and application. *Mechanical Systems and Signal Processing* 40(2), 401-420.

Javadi, A. and H. Nilsson (2017). Detailed numerical investigation of a Kaplan turbine with rotor-stator interaction using turbulence-resolving simulations. *International Journal of Heat and Fluid Flow* 63.

Ketata, A., Z. Driss and M. S. Abid (2020). Impact of blade number on performance, loss and flow characteristics of one mixed flow turbine. *Energy* 203.

Kim, H. H., M. Rakibuzzaman, K. Kim and S. H. Suh (2019). Flow and fast fourier transform analyses for tip clearance effect in an operating kaplan turbine. *Energies* 12(2).

Krüger, S., Y. A. Bouziad and W. Maurer (n.d.). *Pump sump cfd for vertical pump design*. In *ASME 2009 Fluids Engineering Division Summer Meeting*, Vail, Colorado, USA.

Li, X. B., M. Binama, W. T. Su, W. H. Cai, A. Muhirwa, B. Li and F. C. Li (2020). Runner blade number influencing RPT runner flow characteristics under off-design conditions. *Renewable Energy* 152.

Li, Y., I. E. Ohiemi, P. Singh and Y. Sunsheng (2022). Numerical and experimental analysis of pressure fluctuation in axial flow turbine. *AIP Advances* 12(2), 025122.

Menter, F. (1993, July 6). Zonal two equation k-w turbulence models for aerodynamic flows. In *23rd Fluid Dynamics, Plasmadynamics, and Lasers Conference*.

Ni, D., N. Zhang, B. Gao, Z. Li and M. Yang (2020). Dynamic measurements on unsteady pressure pulsations and flow distributions in a nuclear reactor coolant pump. *Energy* 198, 117305.

Ohiemi, I. E., Y. Sun Sheng, P. Singh and Y. Li (2022). Experimental investigation on the effect of axial gap on performance and unsteady pressure pulsations of low head axial flow hydraulic turbine. *Flow Measurement and Instrumentation*, 88, 102255.

Pochylý, F., M. Haluza, P. Rudolf, M. Habán and M. Hudec (2016). Swirl turbine as a variant of low head propeller turbine. In *19th International Seminar on Hydropower Plants: Flexible Operation of Hydropower Plants in the Energy System*, Vienna, Austria.

Rivetti, A., C. Lucino and S. Liscia (2014). Guide vane influence over pressure fluctuation at the discharge ring in a kaplan turbine: experimental assessment. *American Journal of Hydropower, Water and Environment Sytems* 1, 34-37.

Rodriguez, C. G., E. Egusquiza and I. F. Santos (2007). Frequencies in the vibration induced by the rotor stator interaction in a centrifugal pump turbine. *Journal of Fluids Engineering* 129(11), 1428-1435.

Sang, X., X. Zhou, X. Liu and X. Hao (2017). Radial force within two-stage axial-flow blood pump based on LES. *Journal of Vibroengineering* 19(2).

Shamsuddeen, M. M., J. Park, Y. S. Choi and J. H. Kim (2020). Unsteady multi-phase cavitation analysis on the effect of anti-cavity fin installed on a Kaplan turbine runner. *Renewable Energy* 162.

Shi, L., Y. Yuan, H. Jiao, F. Tang, L. Cheng, F. Yang, Y. Jin and J. Zhu (2021). Numerical investigation and experiment on pressure pulsation characteristics in a full tubular pump. *Renewable Energy* 163, 987-1000.

Singh, P. and F. Nestmann (2009). Experimental optimization of a free vortex propeller runner for micro hydro application. *Experimental Thermal and Fluid Science* 33(6), 991-1002.

Singh, P. and F. Nestmann (2010). Exit blade geometry and part-load performance of small axial flow propeller turbines: An experimental investigation. *Experimental Thermal and Fluid Science* 34(6), 798-811.

Singh, P. and F. Nestmann (2011). Experimental

investigation of the influence of blade height and blade number on the performance of low head axial flow turbines. *Renewable Energy* 36(1), 272-281.

Song, X. and C. Liu (2020). Experimental investigation of floor-attached vortex effects on the pressure pulsation at the bottom of the axial flow pump sump. *Renewable Energy* 145, 2327–2336.

Song, X. and C. Liu (2019). Experimental investigation of pressure pulsation induced by the floor-attached vortex in an axial flow pump. *Advances in Mechanical Engineering* 11(3), 1-13.

Sotoude Haghighi, M. H., S. M. Mirghavami, S. F. Chini and A. Riasi (2019). Developing a method to design and simulation of a very low head axial turbine with adjustable rotor blades. *Renewable Energy* 135, 266-276.

Sotoude Haghighi, M. H., S. M. Mirghavami, M. M. Ghorani, A. Riasi and S. F. Chini (2020). A numerical study on the performance of a superhydrophobic coated very low head (VLH) axial hydraulic turbine using entropy generation method. *Renewable Energy* 147, 409-422.

Šoukal, J., F. Pochylý, M. Varchola, A. G. Parygin, A. V. Volkov, G. P. Khovanov and A. V. Naumov (2015). Selection of axial hydraulic turbines for low-head microhydropower plants. *Thermal Engineering* 62(12), 862-867.

Trivedi, C., M. J. Cervantes, G. Bhupendrakumar and O. G. Dahlhaug (2014). Pressure measurements on a high-head Francis turbine during load acceptance and rejection. *Journal of Hydraulic Research* 52(2).

Wilcox, D. C. (1994). Simulation of transition with a two-equation turbulence model. *AIAA Journal* 32(2).

Yasuda, T., A. Funakubo, F. Miyawaki, T. Kawamura, T. Higami and Y. Fukui (2001). Influence of static pressure and shear rate on hemolysis of red blood cells. *ASAIO Journal* 47(4), 351-353.

Yu-qin, W. and D. Ze-wen (2020). Influence of blade number on flow-induced noise of centrifugal pump based on CFD/CA. *Vacuum* 172.

Zhang, M., D. Valentín, C. Valero, M. Egusquiza and E. Egusquiza (2019). Failure investigation of a Kaplan turbine blade. *Engineering Failure Analysis* 97.

Zhang, M., D. Valentin, C. Valero, A. Presas, M. Egusquiza and E. Egusquiza (2020). Experimental and numerical investigation on the influence of a large crack on the modal behaviour of a Kaplan turbine blade. *Engineering Failure Analysis* 109.

Zhu, X., M. Zhang, G. Zhang and H. Liu (2006). Numerical investigation on hydrodynamics and biocompatibility of a magnetically suspended axial blood pump. *ASAIO Journal* 52(6), 624-629.

APPENDIX

A1: Runner Design Using the Free Vortex Theory

The AFT's runners were designed using the free vortex theory derived from the conservation of angular momentum. The free vortex theory is represented by Eq. (A1):

$$v_u \cdot r = K \tag{A1}$$

The free vortex law requires the product of the tangential velocity and the radius vector along the inlet and outlet of the blade to be constant, as shown in Eq. (A2):

$$[v_u \cdot r]_{\text{inlet}} = K_{\text{inlet}}, \text{ and }, [v_u \cdot r]_{\text{exit}} = K_{\text{exit}} \tag{A2}$$

Fig. A1 depicts the inlet velocity triangle of the runner. Under ideal conditions, the tangent velocity v_u value of the exit is 0. At this point, $K_{\text{exit}} = 0$. The v_u decreases with the increase in the radial vector from hub to tip of the runner, which leads to the different liquid flow angles entering each radial section.

The v_m can be represented as

$$v_m = \frac{4Q}{\pi D_t^2 (1-\xi^2)} \tag{A3}$$

According to the Euler equation in a hydraulic turbine, K can be obtained from the following equation:

$$u(v_{u1}-v_{u2}) = gH_T \tag{A4}$$

When $v_{u2} = 0$, u = rw,

$$K = \frac{gH_T}{\omega} \tag{A5}$$

Table A1 shows the cord length and inlet liquid flow angle at each radial position of the runner used in this

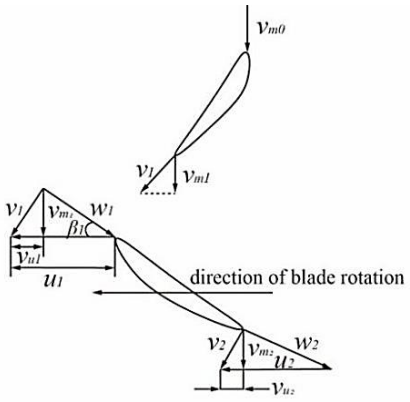

Fig. A1 Inlet velocity triangle of runner

Table A1 Cord length of blade and inlet flow angle.

Diameter Ratio *d*/*D*	Length of Cord *l*	Inlet Flow Angle β
0	85.5	47.7
0.25	100	35.3
0.5	114.5	28.1
0.75	121.5	23.6
1	107	20.1

paper. In general, the inlet position of the blade of an axial-flow turbine adopts a certain positive incidence angle, which, on the one hand, can improve the cavitation performance of the inlet position and, on the other hand, can be well adapted to operate under the condition of large flow, and it has little effect on the efficiency of hydraulic turbine.

A2: Uncertainty Analysis

The rant operating test rig conforms with both worldwide IEC60193-1999 and Chinese national norms, according to certification from Jiangsu province's technical department. The uncertainty resulting from experimental efficiency is calculated in accordance with the IEC60193 hydraulic requirements for performance test acceptance by using Eq (A6).

$$U_i = \sqrt{U_Q{}^2 + U_H{}^2 + U_N{}^2 + U_M{}^2} \tag{A6}$$

where U_Q, U_H, U_N, and U_M stand for the uncertainties in the flow rate, head, rotation speed, and torque, respectively, and U_i represents the system's random uncertainty. Eq.(A7) calculates the component's individual uncertainty measure.

$$U = \sqrt{U_{sys}{}^2 + U_{ran}{}^2} \tag{A7}$$

Utilizing the general coefficient and Bessel technique, respectively, U_{ran} and U_{sys} were calculated. Table A2 presents a thorough report of the uncertainty analysis.

The overall efficiency was determined to be 0.612%; however, this uncertainty is doubled to provide an additional total uncertainty of 1.223% in order to take into account any further uncertainties that may occur. In summary, this experiment complies with accepted accuracy standards.

Table A2 Analysis of Experimental Uncertainty

		Discharge (l/s)	Head (m)	Torque	Shaft Speed (r/min)
No. of Test	1	177.91	3.033	3.539	1450.01
	2	178.23	3.05	3.569	1450.06
	3	177.82	3.246	4.001	1449.2
	4	177.95	3.248	4.024	1450.03
	5	177.82	3.246	4.001	1450.03
Random Uncertainty	Mean Value	177.94	3.165	3.827	1450
	Standard deviation (%)	0.168	0.113	0.249	0.373
	U_{ran} (%)	0.27	0.065	0.144	0.215
System Uncertainty	Measurement accuracy	0.199	0.007	0.449	0
	U_{sys} (%)	0.2	0.1	0.3	0.3
Total uncertainty	Components U (%)	0.336	0.119	0.333	0.369
	Total Uncertainty U (%)	0.612			
Extra total uncertainty U_{ext} (%)		1.223			